Dalton Transactions

RSCPublishing

PAPER

View Article Online
View Journal | View Issue

Cite this: *Dalton Trans.*, 2013, **42**, 11271

Controlling the morphology and pore size of mesostructured silica nanoparticles: the role of the iron oxidation state

Jakelyne Viana Coelho,[a] Marina Silva Guedes,[a] Deicy Barrera,[b] Karim Sapag,[b] Márcio César Pereira*[c] and Luiz Carlos Alves de Oliveira[a]

Received 24th March 2013,
Accepted 4th June 2013

DOI: 10.1039/c3dt50794g

www.rsc.org/dalton

We demonstrate morphology and pore size dependence of silica nanoparticles (SNPs) synthesized *via* control of the iron oxidation state. In the absence of any Fe species, only spherical SNPs are produced, whereas in the presence of Fe^{3+} and Fe^{2+} ions, SNPs with rod-like and nanosheet morphologies, respectively, are formed. The average pore size increases from 1.7 nm in the absence of iron to 3.2 and 5.9 nm as Fe^{3+} and Fe^{2+}, respectively, were used during the synthesis. Both samples of SNPs synthesized in the presence of Fe^{2+} and Fe^{3+} have 0.2 wt% of tetrahedral iron in the silica framework, whereas most of the iron is in the silica extraframework, as verified by Mössbauer spectroscopy, UV-vis diffuse reflectance, FTIR, XRD data and TPR analysis. These Fe^{2+} and Fe^{3+} cations play a fundamental role in controlling these properties because they change the curvature and the surface charge density of CTAB micelles, thus favoring the spherical to rod-like transition. The rod-like shape was retained in Fe^{3+}-containing samples, whereas a nanosheet-like morphology was produced in Fe^{2+}-containing samples due to the breakage of silica walls during the thermal treatment to remove the template. The control of the textural properties is interesting to allow the fabrication of selective photocatalysts for oxidation of different organic substrates.

1. Introduction

Since the discovery of highly ordered mesoporous silica by researchers at Mobil Oil Research and Development in 1992,[1] the synthetic approach to produce these materials has been focused on controlling the morphologies and pore sizes of nanoparticles aiming to tune their properties for particular applications such as catalysis, drug delivery systems, adsorption, photonics, sensors, and controlled release materials.[2–6] Synthesis of silica nanoparticles (SNPs) with different morphologies is also of great interest because important information about porous system engineering can be obtained from these materials. Thus, the knowledge of the synthesis methods and parameters that affect the pore sizes and the morphologies of SNPs still is of great significance for diverse fields of science.

Mesoporous SNPs are usually prepared by using the sol–gel chemistry in the presence of amphiphilic molecules (surfactants) that act as structure directing agents (SDA) for the *in situ* polymerization of a silica source. Because of some molecular environments such as steric effects, hydrophilicity, and van der Waals interactions, the SDA molecules tend to self-assemble to produce thermodynamically stable mesopores. After the silica polymerization step the surfactant molecules are removed by calcination or extraction methods to expose the pore structure of silica.[3,7,8]

Diverse strategies based on changing parameters, such as temperature, solvents, pH, silica sources, surfactant-type, concentration and presence of additives such as salts, co-solvents, co-surfactants and swelling agents, have been used in order to control the pore size and morphology of SNPs.[2–6] By controlling the pH, Zhang *et al.*[9] showed that solid silica spheres can be synthesized at pH values around 12.3, whereas hollow silica spheres are formed at pH values of 12.8. Silica nanotubes with curly or coiled morphology can be synthesized using bacterial flagella as a biotemplate at pH ~ 4. At pH values in the range of 8–11.5 the silica nanotubes can present curly, coiled, straight or sinusoidal morphologies.[10] Straight silica fibers can be prepared by changing the concentration of tetramethyl orthosilicate (TMOS), used as a silica source, whereas silica discoids and spheres with pore size in the range of 2.2–2.6 nm

---

[a] *Departamento de Química, ICEx, Universidade Federal de Minas Gerais, 31270-901 Belo Horizonte, Minas Gerais, Brazil*
[b] *Departamento de Física, Universidad Nacional de San Luis, Chacabuco 917, San Luis, Argentina*
[c] *Instituto de Ciência, Engenharia e Tecnologia, Universidade Federal dos Vales do Jequitinhonha e Mucuri, 39803-371 Teófilo Otoni, Minas Gerais, Brazil. E-mail: mcpqui@gmail.com; Fax: +55 33 3522-6037*

can be prepared by controlling acidity in the sol synthesis.[11] Chemical control of the hydrolysis and condensation steps through pH variation have been shown by Fidalgo *et al.*,[2] and it allows us to prepare monolithic silica with a bimodal pore structure and narrow mesopore size distribution (average pore diameter of 8 nm). Silica with a smaller pore size can be fabricated at low pH due to the formation of thinner walls between pores and to a larger shrinking of the structure upon thermal treatment to remove the template.[12,13]

Wang *et al.*[14] reported that using additives such as ethanol, *n*-butanol, hexanol or 1-octanol during the silica synthesis in the presence of anionic surfactants, hexagonal mesoporous silica discs and particles with multi-layered inner structure are produced. In the absence of these alcohols, only spherical SNPs are obtained. By the control of the water–acetone molar ratios in the presence of cetyltrimethylammonium bromide (CTAB) as a cationic surfactant, it is possible to synthesize mesoporous silica with an average pore size ranging from 2.7 to 3.3 nm and the SNPs can exhibit shapes of nanocoons, nanorods or nanospheres.[15] Silica nanospheres, nanoellipsoids, helical nanorods and multi-lamellar nanovesicles have been prepared by tailoring the weight ratio of CTAB and sodium bis(2-ethylhexyl) sulfosuccinate (AOT) used as co-surfactants.[16] Mesoporous silica with worm-like shapes was synthesized using ionic liquid 1-hexadecane-3-methylimidazolium bromide as a template at high temperature (150–190 °C) and NaF as an additive.[17] The addition of salts on the synthesis gel influences directly the properties of the resulting mesoporous silica. Husson and Luzzati[18] showed that some surfactants change their micellar shape from sphere to rod-like after the addition of salts during the sol synthesis. Huh *et al.*[19] showed that the silica precursor also strongly influences the silica nanoparticle shape. By changing the precursor or its concentration, the particle can have spherical, tube or rod shapes.

As described above, the influence of the pH, temperature, surfactant-type, and silica source on the morphology and pore size of the silica nanoparticles is very well documented. However, to the best of our knowledge, the literature still lacks work dealing with the influence of the oxidation state of metal cations on the morphology and pore size of SNPs.

In the present work, we report the effect of Fe^{2+} and Fe^{3+} cations on the morphology and pore size of mesostructured SNPs, using CTAB as an SDA and tetraethyl orthosilicate (TEOS) as a silica source, in an alkaline medium. The control of the morphology and pore size of SNPs by using Fe^{2+} or Fe^{3+} precursors allows the fabrication of selective photocatalysts to oxidize different organic substrates in water.

2. Experimental

2.1 Materials

Cetyltrimethylammonium bromide (CTAB, >99%) was supplied by Vetec. Sodium hydroxide (>97%), tetraethyl orthosilicate (TEOS, 99.99%), hydrochloric acid (37%), iron(III) chloride hexahydrate (97%) and iron(II) chloride tetrahydrate (98%) were obtained from Sigma-Aldrich.

2.2 Synthesis of the mesoporous silica

Undoped mesoporous SNPs were prepared by dissolving 1.63 g (4.47 mmol) of CTAB in a mixture of 30 g of deionized water and 10 mL of 1 M NaOH, followed by the addition of 3.7 mL (17.0 mmol) of TEOS under stirring at 25 °C. The mixture was then stirred at 25 °C during 24 h at pH 11. After this time period, the pH of the suspension was adjusted to 7 by the addition of 1 M hydrochloric acid. The white precipitates were collected by centrifugation, washed with deionized water three times, and dried at room temperature. To remove the surfactant, 1 g of solid material was calcined in an electrical furnace at 600 °C for 5 hours under air flow (100 mL min^{-1}). This sample was labeled S0.

The Fe(III)-containing SNPs were obtained by the same procedure described for the synthesis of undoped SNPs, except for the addition of (i) 0.12 g (0.6 mmol) $FeCl_2·4H_2O$ to a mixture of CTAB, water, NaOH and TEOS; this sample was labeled S2 and (ii) 0.16 g (0.6 mmol) $FeCl_3·6H_2O$ to a mixture of CTAB, water, NaOH and TEOS; this sample was labeled S3.

2.3 Characterization

The transmission electron microscopy (TEM) images of all samples were taken with a JEOL transmission electron microscope model JEM 2000EXII. Scanning electron microscopy (SEM) images were obtained with a JEOL analyzer coupled to an Oxford (EDS/INCA 350) energy dispersive X-ray analyzer. X-ray diffraction (XRD) was carried out using Cu-Kα radiation with a Rigaku Geigerflex diffractometer equipped with a graphite diffracted-beam monochromator. Data were collected from 3–10° and 10–40° 2θ in steps of 0.02° per 5-s iteration. Mössbauer spectra were collected in constant acceleration transmission mode with a 20 mCi $^{57}Co/Rh$ source. The spectra of all samples were taken at 298 K and 80 K using a liquid nitrogen bath cryostat. The data were stored in a 512 channel MCS memory unit and were fitted using the NORMOS program. Isomer shifts were calculated relative to α-Fe. Diffuse reflectance measurements were performed using a UV-vis spectrometer Cary 5E coupled with a diffuse reflectance accessory from 200 to 800 nm. Teflon powder was used as reference material (100% transmission), and the Kubelka–Munk equation was used to manipulate all data. Fourier transform infrared spectroscopy (FTIR) was performed using a Digilab Ex-calibur Series FTS 3000 instrument with samples diluted in KBr (1% g g^{-1}) in the spectral range of 400–4000 cm^{-1} with a resolution of 8 cm^{-1} and 32 scans. Surface areas were determined by the BET method using a 22 point N2 adsorption/desorption procedure in an Autosorb 1 Quantachrome gas sorption analyzer. The temperature programmed reduction (TPR) analysis was carried out in a CHEM BET 3000 TPR using H_2 (8% in N_2) with a heating rate of 10 °C min^{-1}.

2.4 Photocatalytic tests

80 mL of a 100 mg L^{-1} congo red or methyl orange at pH 6.5 was mixed with 30 mg of the catalyst and irradiated with a 15 W $\lambda < 300$ nm UV lamp. Reactions were monitored by UV-vis spectroscopy (Cary 5E) in the range of 400–800 nm with water circulating through a temperature-controlled bath kept at 25 ± 1 °C.

3. Results and discussion

3.1 Characterization of SNPs

The effect of the addition of Fe^{2+} or Fe^{3+} cations during the synthesis of SNPs on its morphology was evaluated through SEM and TEM images shown in Fig. 1. SEM images of samples S0 and S3 (Fig. 1a and c) reveal only agglomerated particles with undefined shapes, whereas a lamellar morphology was observed for sample S2 (Fig. 1e). On the other hand, TEM images (Fig. 1b, d and f) clearly show that the morphology of SNPs depends strongly on if Fe^{2+} or Fe^{3+} cations are added or not during the synthesis. Fig. 1b shows that solid spherical SNPs are formed if no iron is added during the synthesis (sample S0). When the SNPs are synthesized in the presence of Fe^{3+} ions, irregular nanorods are produced (Fig. 1d), suggesting that the addition of Fe^{3+} cations induces the formation of rod-like micelles as templates and because of this the Fe-SNPs exhibited rod-like morphology. If Fe^{2+} cations are used instead of Fe^{3+} during the synthesis, Fe-SNPs with nanosheet morphologies are produced.

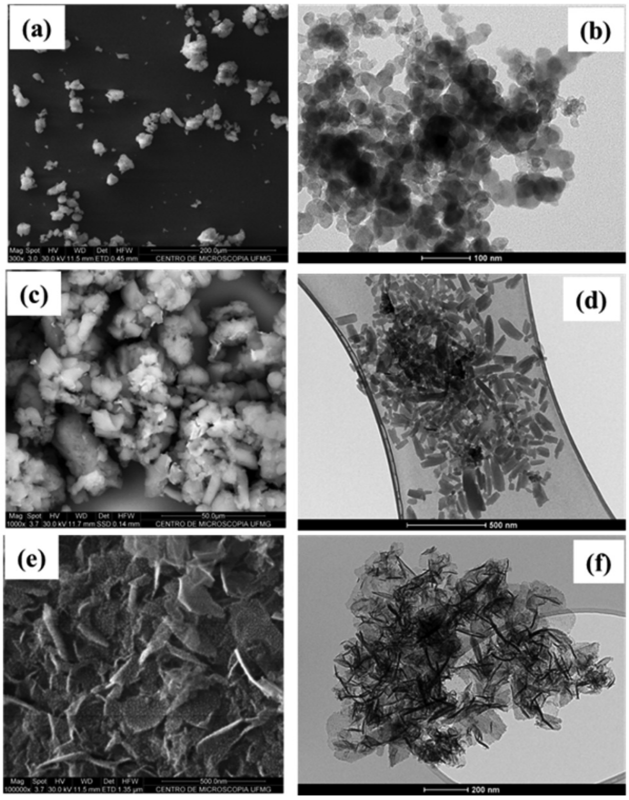

Fig. 1 SEM images of samples (a) S0, (c) S3 and (e) S2. TEM images of samples (b) S0, (d) S3 and (f) S2.

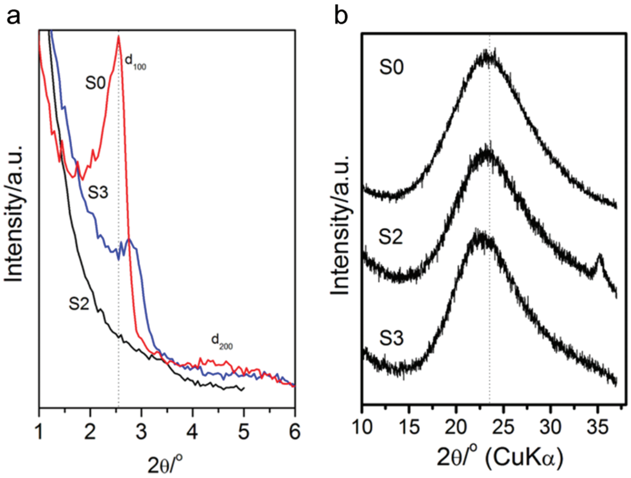

Fig. 2 (a) Powder XRD patterns for the samples S0, S2 and S3. (b) Powder XRD patterns for the samples S0, S2 and S3.

In order to understand the origin of the change in the morphology and the real composition of samples S0, S2 and S3, all of these samples were characterized by several techniques. The XRD patterns of all samples in the range of 1–6° 2θ are shown in Fig. 2a. The diffraction peak (d_{100}) at around 2.5° 2θ in the low angle region of sample S0 suggests the existence of some hexagonal order in the intra-particle mesoporous material. An incipient peak at around 4.7° relative to d_{200} suggests poor hexagonal geometry and periodicity of the mesoporous channels in the sample S0. The XRD pattern of sample S3 revealed that the presence of Fe^{3+} during the synthesis of silica gel strongly affects the hexagonal symmetry of silica, as can be verified by the decrease in the relative intensity of the reflection d_{100} as compared to the same peak in the sample S0. Moreover, the peak (100) is shifted, indicative of some isomorphical substitution of Si^{4+} by Fe^{3+} in the silica framework. If Fe^{2+} ions were used as precursors (sample S2) instead of Fe^{3+} no reflection could be observed in the XRD pattern at low angle, suggesting that the Fe^{2+} ions caused a collapse of the hexagonally ordered silica structure.

The XRD patterns of samples S0, S2 and S3 in the range of 10–38° 2θ (Fig. 2b) show a broadening peak, centered at around 23.5° 2θ, which corresponds to amorphous silica. This peak is shifted to 23.1 and 22.7° 2θ in the S2 and S3 samples, respectively, indicative of isomorphic substitution of Si^{4+} by Fe^{3+} in the silica framework. The tetrahedral coordination ionic radius of Si^{4+} is 49 pm, whereas the Fe^{2+} and Fe^{3+} have 63 and 49 pm in tetrahedral coordination, respectively. Therefore, the replacement of Si by Fe would lead to an increase in the unit cell of silica, as evidenced by the 2θ degree shift to lower angles. In addition to amorphous silica, sample S2 exhibited a broadening reflection at around 35° 2θ, which is characteristic of iron in the extraframework of silica. According to card JCPDS # 3-812 this reflection can be assigned to the most intense 104 peak of hematite that was formed probably due to the calcination process at 600 °C to remove the surfactant. Reflections at angles higher than 40° 2θ were not observed, due to the small amount of Fe in these samples. Using the Scherrer equation, the mean crystallite dimension of hematite nanoparticles obtained from the 104 reflection in the sample S2 was 12 ± 3 nm. For the sample S3, it was not possible to estimate the crystallite dimension, but it is surely lesser than 12 nm, as verified from the amorphous contribution in the range of 28 to 35° 2θ in the XRD pattern of this sample.

UV-vis spectroscopy has been used extensively to characterize the nature and coordination of Fe^{3+} ions in Fe-SNPs.[20–24] Thus, we have used UV-vis spectroscopy in an attempt to distinguish between octahedral and tetrahedral Fe^{3+} in the prepared samples, and then separate iron in the framework and the extraframework of silica. The UV-vis diffuse reflectance spectra in the wavelength range of 200–800 nm of all samples are shown in Fig. 3. Sample S0 showed a low absorption band at a wavelength range of 200–300 nm, which is due to $O^{2-} \rightarrow Si^{4+}$ charge transfer transitions. Amama *et al.*[20] have reported that isolated tetrahedral coordination Fe^{3+} ions absorb radiation in the wavelength range of 200–330 nm with a distinct band at ~260 nm, whereas Fe species in octahedral coordination exhibit a broad absorption band around 320–640 nm with an absorption maximum at ~500 nm. Fig. 3 shows that both samples, S2 and S3, present a shoulder that was fitted with a Gaussian (straight line) centered at 260 nm, which is related to the oxygen ligand for metal charge-transfer transitions associated with Fe^{3+} species in isolate tetrahedrally coordinated sites.[25,26] This is strong evidence for that part of the iron which is incorporated into the silica framework forming Fe–O–Si bonds. On the other hand, the absorption bands higher than 320 nm are indicative of the presence of Fe^{3+} species in octahedral coordination in the samples S2 and S3 because of the formation of extraframework iron oxide. The absorption bands at 434 and 510 nm in the samples S3 and S2, respectively, are due to double excitation processes of two Fe^{3+} cations adjacent and magnetically coupled in the hematite (ideal formula, α-Fe_2O_3) structure.[27] This band is sensitive to the decrease in the particle size and tends to shift to the blue region.[28] Moreover, the lower absorption band value of double Fe^{3+} excitation in the sample S3 suggests that hematite nanoparticles in this sample have stronger interactions with silica walls and are much more dispersed in the pores of silica than in sample S2.

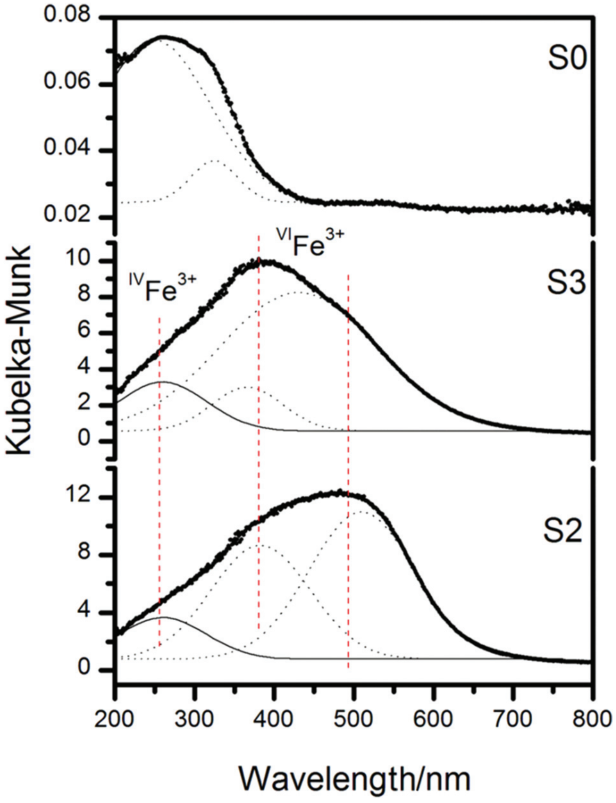

Fig. 3 UV-vis diffuse reflectance of samples S0, S3 and S2.

To define the type of band-to-band transition in the prepared samples, the absorption data were fitted to functions for both direct and indirect transitions. From Tauc's law,[29] an expression that describes the near-edge region of an absorption in semiconductors with indirect band-gap transitions, the absorption edge energies for all samples were estimated by plotting the function $[F(R_\infty)h\nu]^{1/2}$ *versus* $h\nu$, where $F(R_\infty)$ is the Kubelka–Munk function and $h\nu$ is the energy of the incident photon. Based on the expression $[F(R_\infty)h\nu]^{1/2} = C_2(h\nu - E_g)$, the band gap energy ($E_g$) was readily obtained from the linear fit. For direct transition, a plot of $[F(R_\infty)h\nu]^2$ *versus* $h\nu$ was used.[30] As shown in Fig. 4a for samples S0, S2 and S3, the indirect fit plot yields band gap values of 2.6, 1.8 and 1.8 eV, respectively, which does not seem realistic because (i) silica does not absorb visible radiation and (ii) the band gap energy for bulk hematite is reportedly ~2.0 eV.[31] The hematite nanoparticles in samples S2 or S3 are smaller than those in the bulk hematite and, therefore, the band gap energy would be expected to

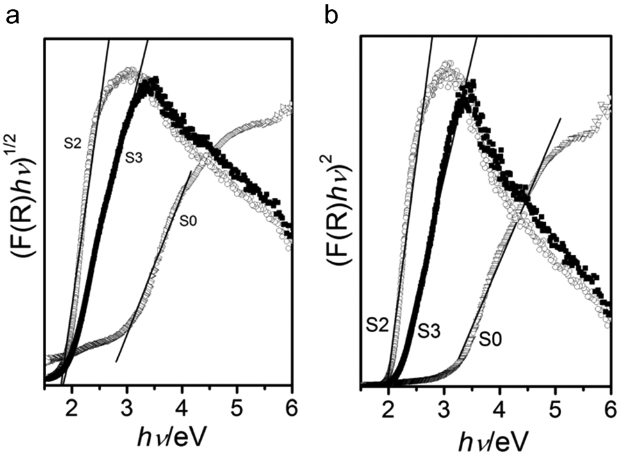

Fig. 4 (a) $(F(R)h\nu)^{1/2}$ as a function $h\nu$ for the indirect band gap energy determination. (b) $(F(R)h\nu)^2$ as a function $h\nu$ for the direct band gap energy determination.

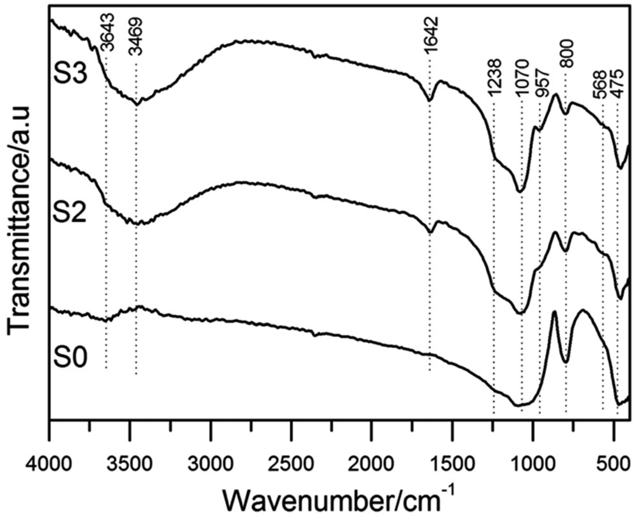

Fig. 5 FTIR for samples S3, S2 and S0.

increase.[32] Thus, the band gap energy in samples S2 and S3 should be at least equal to 2.0 eV and not less as observed in this case. The diffuse reflectance data of all samples may be therefore fitted to a direct band gap function as shown in Fig. 4b. The band gap energies calculated from direct transition are 3.0, 2.0 and 2.1 eV for samples S0, S2 and S3 respectively. These values are more appropriate for pure silica and for Fe-SNPs than those estimated from indirect transitions. As the electronic absorption of iron oxides (hematite) is usually stronger than the absorption of Fe in the silica framework, the determination of electronic transition of Fe-doped silica was not possible at this stage due to band overlaps.

FTIR spectra of all samples are shown in Fig. 5. The broad bands centered at 3469 cm^{-1} for samples S2 and S3 may be attributed to adsorbed water molecules, while deformational vibrations of adsorbed water molecules were observed at 1642 cm^{-1}. The shoulder at around 3643 cm^{-1} can be assigned to the Si–O–H framework, as well as Si(OH)Fe groups in interaction with defect sites in S2 and S3 samples. The absorption band at 1070 cm^{-1} is due to anti-symmetric Si–O–Si vibration. The band at 957 cm^{-1} observed in the S2 and S3 samples is due to an anti-symmetric Si–O–Fe vibration band, indicative of isomorphic substitution of Si by Fe in the silica structure.[33,34] The absorption band at 1238 cm^{-1} is related to asymmetric stretching vibrations of Si–O–Si bridges. The absorption band at around 800 cm^{-1} corresponds to symmetric stretching of Si–O–Si and/or Si–O–Fe vibrations.[35] The relative intensity of this band in samples S2 and S3 is much lower than in sample S0 because of reduction of hexagonal symmetry caused by isomorphic substitution of Si by Fe in the silica framework. The absorption band at around 475 cm^{-1} can be assigned to deformation modes of SiO_4 and/or FeO_4 tetrahedra in the silica structure.[35] This band is slightly shifted to lower wave number values in samples S2 and S3 due to an increase of the mean M–O (M = Si or Fe) distance in the silica walls caused by introduction of Fe into the silica network.[34] The observed shifts, 455 and 449 cm^{-1} in samples S2 and S3 against 475 cm^{-1} in sample S0, depend on the change in the ionic radii and the amount of iron doping. As the observed shifts are comparatively small, we suggest that the cation substitution degree in silica structure is low. The shoulder at 568 cm^{-1} in samples S2 and S3 is due to Fe–O vibration of hematite.

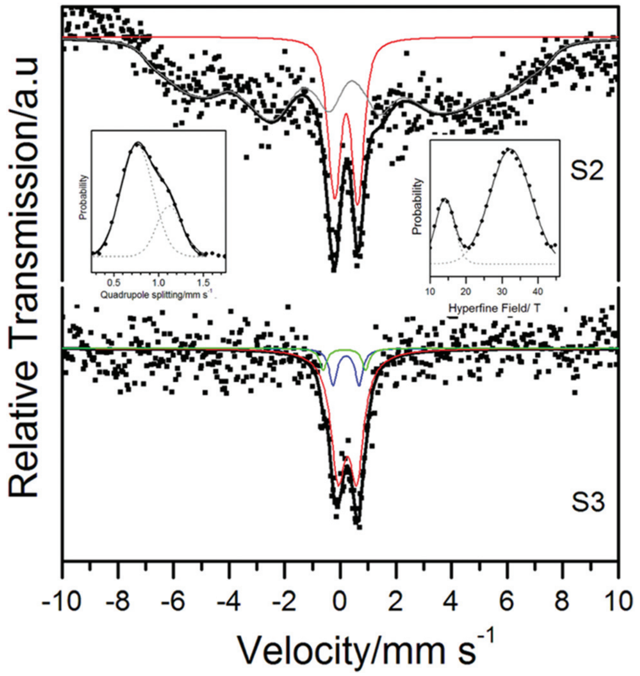

Fig. 6 298 K Mössbauer spectra for samples S2 and S3.

^{57}Fe Mössbauer measurements were carried out to confirm the existence of Fe in the framework and the extraframework of silica, as this technique is specific for the study of the Fe environment. 298 K Mössbauer spectra (Fig. 6) indicated that only Fe in the oxidation state 3+ is present in the samples S2 and S3, suggesting that all Fe^{2+} initially present in sample S2 was converted into Fe^{3+} during the thermal treatment to remove the surfactant. The 298 K Mössbauer spectrum of sample S2 was fitted using one hyperfine field distribution model (Fig. 6, inset) and another one for the quadrupole splitting distribution model (Fig. 6, inset). The hyperfine field distribution (gray line) revealed the existence of two maxima centered at 14.5 and 32.3 T (Fig. 6, inset) corresponding to Fe^{3+} octahedrally coordinated in the extraframework of silica. These hyperfine fields are much lower than that expected for very well crystallized iron oxides due to the small particle size and the high dispersion of these nanoparticles on the silica matrix. Because of this, the Mössbauer spectrum of sample S2 showed asymmetrically broadened lines. Based on the hyperfine parameters (Table 1) obtained from the fit of the spectra we suggest that this magnetically ordered component is due to hematite formed from the oxidation/dehydroxylation of $Fe(OH)_2$ in the silica gel during the calcination process. The two paramagnetic components obtained from the quadrupole

Table 1 Hyperfine field parameters of the spectra of samples S2 and S3 collected at 298 and 80 K. δ = isomer shift relative to α-Fe, ε = quadrupole shift, Δ = quadrupole splitting, B_{hf} = magnetic hyperfine field, RA = relative subspectral area

Sample	δ (mm s^{-1})	ε, Δ (mm s^{-1})	B_{hf} (T)	RA (%)	^{57}Fe site
298 K					
S2	0.32	0.71	—	15	Fe^{3+}
	0.31	1.04	—	5	Fe^{3+}
	0.38	−0.21	32.3	80	$^{VI}Fe^{3+}$
S3	0.37	0.67	—	80	$^{VI}Fe^{3+}$
	0.32	0.93	—	13	Fe^{3+}
	0.26	1.52	—	7	$^{IV}Fe^{3+}$
80 K					
S2	0.48	−0.21	50.6	76	$^{VI}Fe^{3+}$
	0.46	0.83	—	20	$^{VI}Fe^{3+}$
	0.36	1.46	—	4	$^{IV}Fe^{3+}$
S3	0.47	0.79	—	79	$^{VI}Fe^{3+}$
	0.43	1.36	—	15	Fe^{3+}
	0.36	1.90	—	6	$^{IV}Fe^{3+}$

splitting distribution (Fig. 6, inset) have an isomer shift value (Table 1) between octahedral and tetrahedral sites, which suggest a strong interaction between the silica support and the hematite nanoparticles. At least at this temperature it was not possible to define iron in tetrahedral positions. The Mössbauer spectrum of sample S3 does not show clearly any magnetic ordering at 298 K, indicative of the formation of ultrafine particles on the extraframework silica and/or Fe in the silica structure. The spectrum was fitted with three doublets that correspond to superparamagnetic hematite (Δ = 0.67 mm s^{-1}, Table 1), superparamagnetic hematite with strong interaction with the silica walls (Δ = 0.93 mm s^{-1}) and in minor extension, Fe^{3+} in tetrahedral (Δ = 1.52 mm s^{-1}) into the silica framework. The high quadrupole splitting value of this component indicates distortion of the SiO_4 tetrahedra due to isomorphic substitution of Si^{4+} by Fe^{3+}.

In order to minimize the superparamagnetic relaxations observed at room temperature, Mössbauer spectra were collected at 80 K. The obtained spectra (Fig. 7) were very similar to those collected at 298 K. From the hyperfine parameters shown in Table 1, it was possible to establish that Fe in sample S2 is located in hematite and in the silica structures. The iron in the silica structure was identified by the presence of tetrahedral Fe^{3+} (green line, Fig. 7), whereas two types of hematite were verified:

(i) hematite with higher particle size (gray line, Fig. 7; B_{hf} = 50.6 T, Table 1) and (ii) hematite ultradispersed and with strong interaction with the silica walls (Fig. 7, blue line), as the isomer shift lies between the expected values for octahedral and tetrahedral sites. The 80 K Mössbauer spectrum of sample S3 (Fig. 7) also confirms the Fe in the silica framework and extraframework. However, the hematite is much more disperse on the silica structure in sample 3 than in sample S2, as no magnetic ordering was observed even at 80 K. As in sample S2, it was possible to distinguish among Fe^{3+} in hematite (red line), hematite with strong interaction (blue line) with silica walls and Fe^{3+} in tetrahedral sites of silica.

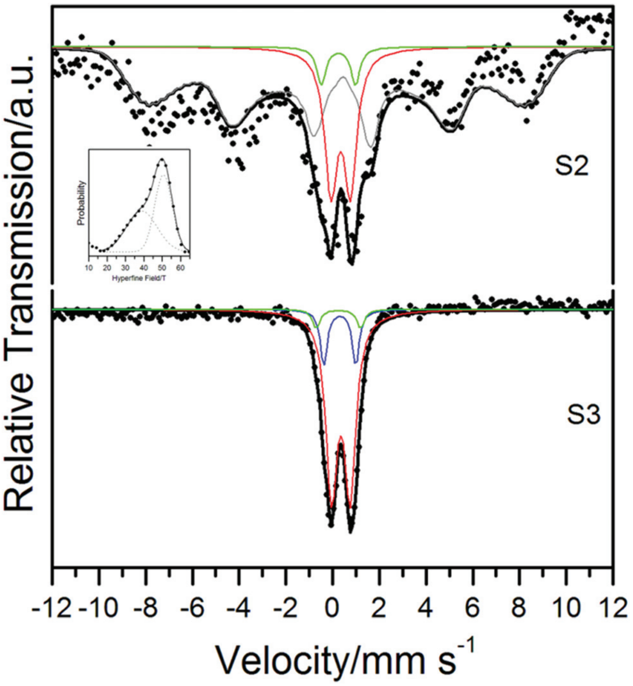

Fig. 7 80 K Mössbauer spectra for samples S2 and S3.

Based on the total Fe chemical analysis and in the Mössbauer relative areas (Table 1) it was possible to estimate the amount of iron in the framework and the extraframework of the silica. The total Fe content obtained with AAS analysis was 4.4(2) and 2.6(2) wt% for samples S2 and S3, respectively. Thus, the iron in sample S2 can be determined as 3.3 wt% due to hematite, 0.9 wt% hematite with strong interaction with the silica walls and 0.2 wt% in the silica structure, whereas for sample S3 the iron content in hematite, hematite (strong interaction) and in the silica structure was determined as 2.0, 0.4 and 0.2 wt%, respectively.

The reduction of iron ions present in the SNPs was investigated by measuring the hydrogen uptake with increasing temperature. The TPR profiles of samples S0, S2 and S3 are shown in Fig. 8 and it allows us to estimate the reducibility of iron species,[36,37] which depends on the interaction between the iron and the silica matrix. It is characteristic that the impregnated iron species exhibits the much easier reduction of iron than iron in the silica framework. Thus, strong Fe interaction with silica should be achieved when iron is introduced during the template synthesis. The sample S0 exhibited only one reduction peak centered at 765 °C that can be assigned to reduction of Si–OH groups in the silica.[38] The samples S2 and S3 exhibited a small peak centered at 223 °C related to the reduction of ultrafine hematite nanoparticles on the silica surface. The peak at 436 °C in the sample S2 is also due to the reduction of hematite into magnetite. That peak is shifted to 452 °C in sample S3, indicating strong iron oxide interaction with the silica matrix. This peak is more broadened than the same peak for sample S2, due to higher dispersion of hematite nanoparticles in sample S3. Pereira *et al.*[39] reported that the

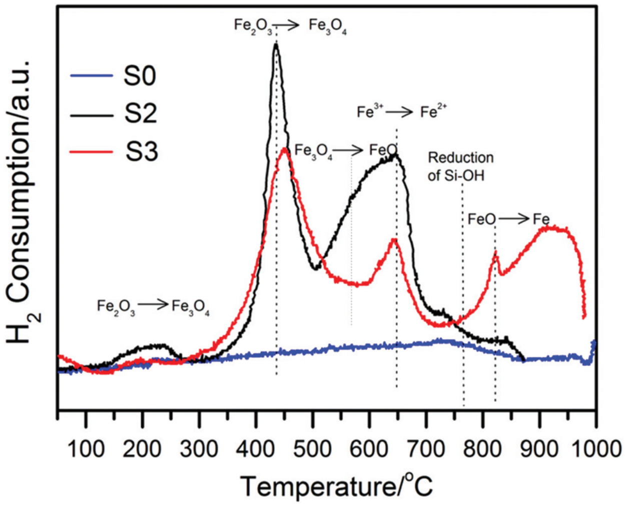

Fig. 8 TPR profiles for the samples S0, S2 and S3.

Table 2 Hyperfine field parameters of the spectra of samples S2 and S3 collected at 298 K, after reduction with H_2. δ = isomer shift relative to α-Fe, ε = quadrupole shift, Δ = quadrupole splitting, B_{hf} = magnetic hyperfine field, RA = relative subspectral area

Sample	δ (mm s^{-1})	ε, Δ (mm s^{-1})	B_{hf} (T)	RA (%)	^{57}Fe site
S3	0	0	32.9	3	α-Fe
	1.13	2.78	—	62	Fe^{2+}
	0.38	0.88	—	35	Fe^{3+}
S2	0	0	33.1	23	α-Fe
	1.07	2.96	—	34	Fe^{2+}
	0.66	1.76	—	10	Fe^{2+}
	0.38	0.35	—	12	Fe^{3+}
	0.41	1.38	—	21	Fe^{3+}

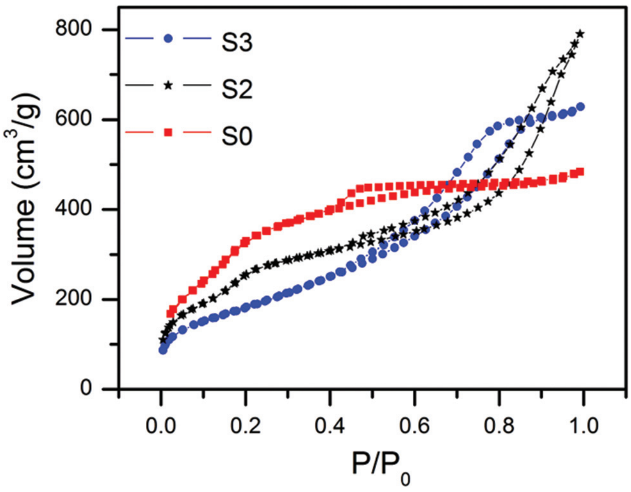

Fig. 10 N_2-adsorption and desorption isotherms for the samples S0, S2 and S3.

transition from hematite to magnetite occurs at approximately 400 °C, and therefore the peak shifts observed in the samples S2 and S3 suggest that the iron oxides strongly interact with the silica walls. The reduction of magnetite to wüstite occurs at around 570 °C, as observed in sample S2. This reduction peak was not observable for sample S3. The peak at 648 °C is due to Fe^{3+} reduction in the silicate structure. This suggests that after 600 °C, the silica changes its structure and instead of magnetite or wüstite directly to reduce to metal iron, the iron in the iron oxide structure migrates to silicate structure in a solid state reaction to produce Fe_2SiO_4. This hypothesis is confirmed by Mössbauer spectra (Fig. 9) collected after the TPR measurements. The spectrum shows that a small part of total, *i.e.* 3 and 23% (Table 2) in samples S3 and S2, respectively, is converted in metallic iron. The remaining 97 and 77% of samples S3 and S2 correspond to iron in the Fe_2SiO_4 structure. This fact is indirect evidence that the iron is strongly attached on the silica matrix in both S2 and S3 samples. The peak at around 821 °C is due to the reduction of FeO to produce metal iron. The fact that most iron is reduced to ferrous cations (not to metallic iron) can be explained by the stabilization of ferrous cations due to their strong interaction with the silica matrix.

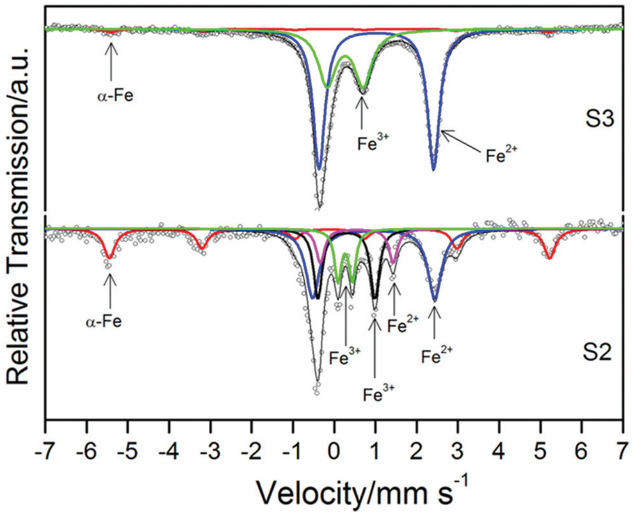

Fig. 9 298 K Mössbauer spectra of samples S3 and S2 after reduction with hydrogen.

The nitrogen isotherms of all samples (Fig. 10) showed type IV features, characteristic of mesoporous material with cylindrical pores. It can be observed that the presence of iron ions in the gel during synthesis lowers the surface areas of the resulting silica from 1406 m^2 g^{-1}, in sample S0, to 911 and 676 m^2 g^{-1} in samples S2 and S3, respectively, likely due to the change in the morphology of nanoparticles with the Fe addition and because of the hematite nanoparticles occupying part of the silica pores. Moreover, the average pore diameter increases with the introduction of iron during the synthesis. Once the same surfactant template was utilized for the synthesis of both pure silica and Fe-SNPs materials, we should expect to obtain average pore diameter in a close range for both types of materials. Nevertheless, our results suggest that the pore diameter can be controlled by using Fe^{3+} or Fe^{2+} ions in the presence of CTAB, as shown in Fig. 11. The average pore

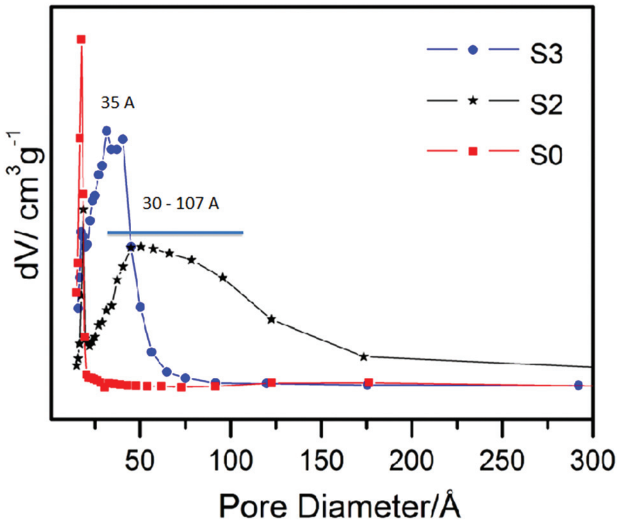

Fig. 11 Pore size distributions curves for the samples S0, S2 and S3.

size distributions of samples S0, S3 and S2 were 1.7, 3.2 and 5.9 nm, respectively. The higher pore size of samples S2 and S3 is likely due to the higher ionic radius of Fe^{2+} and Fe^{3+} ions than the Si^{4+} ions, which causes partial breakage of the tubular walls of the silica structure resulting in the formation of larger pores.

3.2 Synthesis mechanism of solid spheres, rods and nanosheets of SNPs

It is known that in aqueous solution CTAB ionizes to produce micelles with aggregates of CTA^+ ions. Its critical micelle concentration (CMC) is 0.03% (0.9–1.0 mmol L^{-1}). Above the CMC, a transition from spherical micelles to other shaped micelles occurs. Moreover, both adsorbed counterions and surface curvature can change the surface charge density of the surfactant and, therefore, change in the morphology of micelles takes place. For example, CTAB forms spherical micelles in pure water, but in the presence of additives such as NaBr it forms long rod-like and thread-like micelles.[40] To explain the rod-like and nanosheet morphologies as Fe^{3+} or Fe^{2+}, respectively, are added during silica synthesis we propose the following mechanism. Firstly, after the addition of Fe^{3+} or Fe^{2+} salts to the mixture of CTAB, water, NaOH and TEOS the formation of $Fe(OH)_3$ or $Fe(OH)_2$ nanoparticles occurs due to the precipitation reaction. Since the amount of NaOH is much higher than that of Fe^{3+} or Fe^{2+}, the respective hydroxides are surrounded by ^-OH ions, which leads to the adsorption of ^-OH onto the surface of $Fe(OH)_3$ nanoparticles, which results in $Fe(OH)_3$ or $Fe(OH)_2$ negatively charged and the formation of the precursors $Fe(OH)_3\cdot{}^-OH$ (sample S3) or $Fe(OH)_2\cdot{}^-OH$ (sample S2). Secondly, these precursors interact with positively charged CTA^+ head groups through electrostatic interactions to produce $CTA^+–Fe(OH)_3\cdot{}^-OH$, thereby affecting surface charge density of the surfactant. Because of this, the nonpolar core of the droplets tends to decrease and the droplet curvature increases, thus promoting the formation of rod-like micelles. After the thermal treatment, the sample S3 retains the rod-like morphology, whereas the sample S2 is converted into nanosheets due to the breakage of the tubular walls of the silica structure, as verified by the loss of hexagonal symmetry in XRD analysis and by the increase in the pore size shown by BET measurements. The $Fe(OH)_3$ or $Fe(OH)_2$ nanoparticles are needed for the formation of rod-like micelles because the introduction of these species can inhibit the repulsion among the ionic heads of the surfactant giving rise to an increase of the micelle curvature. When no Fe is added to the solution, keeping other experimental conditions constant, solid spherical structures instead of rod- and sheet-like structures are obtained. The proposed mechanism is shown in Fig. 12.

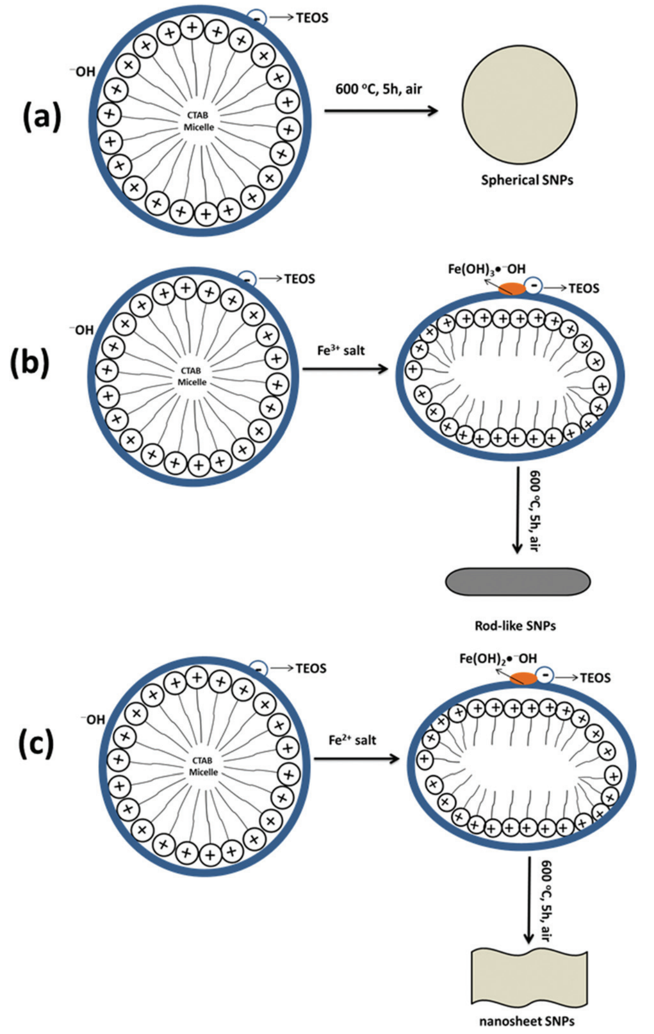

Fig. 12 Schematic representation for the formation of SNPs with (a) spherical, (b) rod-like and (c) sheet-like morphologies.

3.3 Photocatalysis tests

In order to show the applicability of the control of morphology and pore size of SNPs, photocatalytic experiments based on large (congo red) and small (methyl orange) substrates were

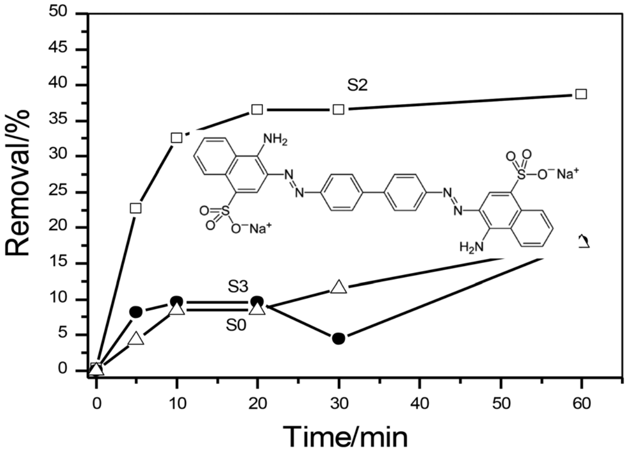

Fig. 13 Photocatalytic removal of congo red in the presence of samples S0, S2 and S3.

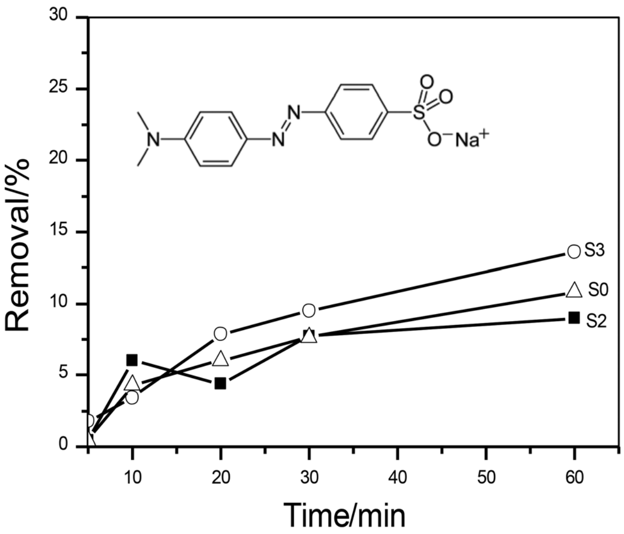

Fig. 14 Photocatalytic removal of methyl orange in the presence of samples S0, S2 and S3.

performed. The results indicated much lower activity of the S3 catalyst (*ca.* 15% of removal after 60 min of reaction) in the removal of congo red than the S2 material (*ca.* 35% of removal after 60 min of reaction) under our experimental conditions (Fig. 13).[41] For the S3 catalyst, pore sizes are smaller than those of S2 as shown in Fig. 11, indicating higher diffusion resistance when a large molecule is used as a substrate. To confirm these results a similar experiment was carried out using a smaller organic dye (methyl orange) as a substrate (Fig. 14). In this case the catalysts presented a similar removal capacity, with approximately 10% of removal after 60 min of reaction. This result indicates that the porosity does not affect the reaction when the substrate is a small molecule. Thus, the results showed that the incorporation of Fe^{2+} (sample S2) or Fe^{3+} (sample S3) into mesoporous SNPs could form a selective catalyst for photocatalysis processes.

4. Conclusions

SNPs with spherical, rod-like and nanosheet morphologies and pore sizes were fabricated by introducing Fe^{2+} or Fe^{3+} salts during the synthesis. These salts are of fundamental importance to control these properties because they change the curvature and surface charge density of micelles favoring the spherical to rod-like transition. The rod-like shape is retained in Fe^{3+}-containing samples, whereas a nanosheet morphology is produced in Fe^{2+}-containing samples due to the breakage of silica walls during the thermal treatment to remove the template. The catalytic activity was strongly affected due to the difference in the pore size caused by the incorporation of Fe^{2+} or Fe^{3+} into the silica matrix. These results show that we can control the textural properties to make an efficient and selective catalyst to remove different types of molecules.

Acknowledgements

The authors are grateful to FAPEMIG, CAPES, CNPq and PRPq/UFMG for financial support.

Notes and references

1 C. T. Kresge, M. E. Leonowicz, W. J. Roth, J. C. Vartuli and J. S. Beck, *Nature*, 1992, **359**, 710–712.
2 A. Fidalgo, M. E. Rosa and L. M. Ilharco, *Chem. Mater.*, 2003, **15**, 2186–2192.
3 F. Tang, L. Li and D. Chen, *Adv. Mater.*, 2012, **24**, 1504–1534.
4 N. Mizoshita, T. Tani and S. Inagaki, *Chem. Soc. Rev.*, 2011, **40**, 789–800.
5 B. G. Trewyn, I. I. Slowing, S. Giri, H. T. Chen and V. S. Y. Lin, *Acc. Chem. Res.*, 2007, **40**, 846–853.
6 G. Øye, W. R. Glomm, T. Vrålstad, S. Volden, H. Magnusson, M. Stöcher and J. Sjöblom, *Adv. Colloid Interface*, 2006, **123–126**, 17–32.
7 G. E. Fryxell, *Inorg. Chem. Commun.*, 2006, **9**, 1141–1150.
8 V. Meynen, P. Cool and E. F. Vansant, *Microporous Mesoporous Mater.*, 2009, **125**, 170–223.
9 H. Zhang, Y. Zhao and D. L. J. Akins, *Solid State Chem.*, 2012, **194**, 277–281.
10 D. Li, X. Qu, S. M. C. Newton, P. E. Klebba and C. Mao, *J. Mater. Chem.*, 2012, **22**, 15702–15709.
11 S. P. Naik, S. P. Elangovan, T. Okubo and I. Sokolov, *J. Phys. Chem. C*, 2007, **111**, 11168–11173.
12 A. C. Voegtlin, A. Matijasic, J. Patarin, C. Sauerland, Y. Grillet and L. Huve, *Microporous Mater.*, 1997, **10**, 137–147.
13 F. Di Renzo, F. Testa, J. D. Chen, H. Combon, A. Galarneau, D. Plee and F. Fajula, *Microporous Mater.*, 1999, **28**, 437–446.
14 W. Q. Wang, J. G. Wang, P. C. Sun, D. T. Ding and T. H. Chen, *J. Colloid Interface Sci.*, 2009, **331**, 156–162.

15 J. Zhang, M. Liu, A. Zhang, K. Lin, C. Song and X. Guo, *Solid State Sci.*, 2010, **12**, 267–273.

16 H. Chen and J. He, *Chem. Commun.*, 2008, **37**, 4422–4424.

17 H. Liu, M. Wang, H. Hu, Y. Liang, Y. Wang, W. Cao and X. J. Wang, *Solid State Chem.*, 2011, **184**, 509–515.

18 F. R. Husson and V. Luzzati, *J. Phys. Chem.*, 1964, **68**, 3504–3511.

19 S. Huh, J. W. Wiench, J. C. Yoo, M. Pruski and V. S. Y. Lin, *Chem. Mater.*, 2003, **15**, 4247–4256.

20 P. B. Amama, S. Lim, D. Ciuparu, Y. Yang, L. Pfefferle and G. L. Haller, *J. Phys. Chem. B*, 2005, **109**, 2645–2656.

21 A. Vinu, D. P. Sawant, K. Ariga, K. Z. Hossain, S. B. Halligudi, M. Hartmann and M. Nomura, *Chem. Mater.*, 2005, **17**, 5339–5345.

22 K. Watanabe and M. Ogura, *Microporous Mesoporous Mater.*, 2008, **114**, 229–237.

23 Y. Wu, Y. Zhang, J. Cheng, Z. Li, H. Wang, Q. Sun, B. Han and Y. Kong, *Microporous Mesoporous Mater.*, 2012, **162**, 51–59.

24 M. Ziolek, I. Nowak, B. Kilos, I. Sobczak, P. Decyk, M. Tredja and J. C. Volta, *J. Phys. Chem. Solids*, 2004, **65**, 571–581.

25 P. Ratnasamy and R. Kumar, *Catal. Today*, 1991, **9**, 329–416.

26 M. C. Pereira, L. C. D. Cavalcante, F. Magalhães, J. D. Fabris, J. W. Stucki, L. C. A. Oliveira and E. Murad, *Chem. Eng. J.*, 2011, **166**, 962–969.

27 B. Li, J. Xu, J. Liu, S. Zuo, Z. Pan and Z. Wu, *J. Colloid Interface Sci.*, 2012, **366**, 114–119.

28 K. M. Reddy, C. C. G. Reddy and S. V. Manorama, *J. Solid State Chem.*, 2001, **158**, 180–186.

29 J. Tauc, in *Amorphous and Liquid Semiconductors*, ed. J. Tauc, Plenum, London, 1974.

30 M. C. Pereira, E. M. Garcia, A. C. Silva, E. Lorençon, J. D. Ardisson, E. Murad, J. D. Fabris, T. Matencio, T. C. Ramalho and M. V. J. Rocha, *J. Mater. Chem.*, 2011, **21**, 10280–10282.

31 R. M. Cornell and U. Schwertmann, *The Iron Oxides - Structure, Properties, Reactions, Ocurrences and Uses*, WILEY-VCH, Weinheim, 2nd edn, 2003, 694p.

32 K. M. Reddy, S. V. Manorama and A. R. Reddy, *Mater. Chem. Phys.*, 2002, **78**, 239–245.

33 M. Selvaraj, B. H. Kim and T. G. Lee, *Chem. Lett.*, 2005, 1290–1291.

34 S. Samanta, S. Giri, P. U. Sastry, N. K. Mal, A. Manna and A. Bhaumik, *Ind. Eng. Chem. Res.*, 2003, **42**, 3012–3018.

35 H. Kosslick, G. Lischke, G. Walther, W. Storek, A. Martin and R. Fricke, *Microporous Mater.*, 1997, **9**, 13–33.

36 I. R. Guimaraes, A. Giroto, L. C. A. Oliveira, M. C. Guerreiro, D. Q. Lima and J. D. Fabris, *Appl. Catal., B*, 2009, **91**, 581–586.

37 W. Ferraz, L. C. A. Oliveira, R. Dallago and L. Da Conceicao, *Catal. Commun.*, 2007, **8**, 131–134.

38 E. P. Reddy, L. Davydov and P. G. Smirniotis, *J. Phys. Chem. B*, 2002, **106**, 3394–3401.

39 M. C. Pereira, F. S. Coelho, C. C. Nascentes, J. D. Fabris, M. H. Araújo, K. Sapag, L. C. A. Oliveira and R. M. Lago, *Chemosphere*, 2010, **81**, 7–12.

40 T. Imae, R. Kamiya and S. Ikeda, *J. Colloid Interface Sci.*, 1985, **108**, 215–225.

41 A. P. L. Batista, H. W. P. Carvalho, G. H. P. Luz, P. F. Q. Martins, M. Goncalves and L. C. A. Oliveira, *Environ. Chem. Lett.*, 2010, **8**, 63–67.